Massive MIMO Beam ID-Based Positioning Method With Low Earth Orbit Satellite Mega Constellations

Mahmoud Elsanhoury, *Member, IEEE*, Janne Koljonen, Fabricio S. Prol, Mohammed S. Elmusrati, *Senior Member, IEEE*, and Heidi Kuusniemi, *Member, IEEE*

***Abstract*—The growth of satellite-based positioning methods has revolutionized global navigation by providing reliable geolocation capabilities. However, traditional Global Navigation Satellite Systems (GNSS) are increasingly vulnerable to threats like jamming, spoofing, and interception, undermining their reliability in critical applications such as in-flight navigation and emergency services. To address these challenges, Low Earth Orbit (LEO) satellite constellations have emerged as a promising complement to GNSS infrastructure. LEO satellites, orbiting at lower altitudes with higher density, offer improved signal availability, reduced degradation, and better reception on Earth. This paper presents a LEO satellite-based positioning method via massive multiple-input multiple-output (mMIMO) beamforming antennas. The proposed technique not only mitigates GNSS vulnerabilities but also introduces a passive sensing mechanism that facilitates positioning without complex timing synchronization, improving resilience in jamming-prone environments. By utilizing LEO satellite beam identifiers as geographic pointers, our method enables precise positioning through LEO satellite ephemeris and beam pattern data. We validate this beam-based method through simulations, LEO constellation data, vehicular drive-test datasets, and probabilistic positioning models. Positioning results from the first dataset show a mean absolute error (MAE) of 9.15 meters and a 95th percentile error (p95%) of 19.07 meters when combining LEO satellite data with inertial motion data from a moving vehicle. Meanwhile, GNSS accuracy was MAE = 26.6 meters and p95% = 56.6 meters. The second dataset showed consistent results with accuracy improvements in MAE from 18.55 to 9.42 meters, RMSE from 22.24 to 12.05 meters, and p95% from 36.38 to 21.18 meters, compared to GNSS. These findings highlight the potential of LEO satellite positioning to improve accuracy and reliability in challenging environments, with implications for critical applications such as remote sensing, emergency response, search and rescue, and situational awareness.**

***Index Terms*—Massive MIMO, radio identification, LEO-PNT, beamforming, navigation and positioning, GNSS, sensor fusion.**

Received 23 March 2025; revised 10 June 2025 and 29 July 2025; accepted 4 August 2025. Date of publication 12 August 2025; date of current version 26 August 2025. This work was supported in part by the Jane and Aatos Erkko Foundation, and in part by the Teknologiateollisuus 100-Year Foundation (INCUBATE Project). *(Corresponding author: Mahmoud Elsanhoury.)*

Mahmoud Elsanhoury, Janne Koljonen, and Mohammed S. Elmusrati are with the School of Technology and Innovations, University of Vaasa, 65200 Vaasa, Finland (e-mail: mahmoud.elsanhoury@uwasa.fi).

Fabricio S. Prol is with the Finnish Geospatial Research Institute, National Land Survey, 02150 Helsinki, Finland.

Heidi Kuusniemi is with the School of Technology and Innovations, University of Vaasa, 65200 Vaasa, Finland, and also with the Finnish Geospatial Research Institute, National Land Survey, 02150 Helsinki, Finland.

Digital Object Identifier 10.1109/JRFID.2025.3598214

I. Introduction

THE SKIES of Earth are becoming increasingly congested with low Earth orbit (LEO) satellites, as mega constellations are projected to surpass tens of thousands in the coming years. Significant cost reductions in LEO satellite design and rocket launches have prompted major corporations to plan the deployment of thousands of satellites into orbit to establish a sustainable presence in the skies and new space economy to emerge. These LEO satellites are primarily developed to extend broadband Internet coverage to rural and signal-deprived areas while also supporting navigation applications for general purposes. A new scenario of research emerged to exploit such Signals-of-Opportunity (SoOp or SOP) and leverage the substantial LEO satellite-to-Earth communications traffic to provide navigational and positioning solutions [1], [2], [3], [4], [5].

Existing global navigation satellite systems (GNSSs), such as GPS, Galileo, GLONASS, and Beidou are widely utilized for high-precision outdoor positioning across various consumer segments. They offer global coverage in the most densely populated regions on Earth and exhibit excellent availability and interoperability, often collaborating with space-based augmentation systems (SBAS) like WAAS and EGNOS. However, GNSS systems operate at much higher altitudes, ranging from medium Earth orbits (MEO) to geostationary Earth orbits (GEO), situated between 2,000 and 35,000 kilometers above sea level. These elevated altitudes result in greater signal degradation due to various factors, first and foremost suffering from atmospheric effects [6], [7]. Additionally, the high altitudes limit the signal ability to penetrate indoor spaces due to substantial shadowing effects caused by obstructions [8], [9]. Furthermore, while GNSS systems are specifically designed for positioning and continue to advance with spoofing and jamming mitigation techniques [10], [11], [12], they remain vulnerable to certain forms of interference, particularly in contested or obstructed environments. In contrast, SoOp although not originally intended for positioning, it can offer complementary capabilities by leveraging their diverse frequency bands, transmission patterns, and spatial characteristics. Exploring SoOp-based positioning methods as a supplement to GNSS represents a promising approach to enhancing navigation resilience, without the need to deploy new LEO constellations dedicated solely to positioning.

In recent years, there has been a noticeable surge in interest surrounding LEO satellites positioning, navigation, and timing

(LEO-PNT) methods [13], [14], largely driven by the number of LEO satellites in the atmosphere. The primary objective of LEO-PNT is to complement existing GNSS by providing enhanced navigation capabilities in challenging scenarios. This includes autonomous navigation, urban environments [15], areas with dense forest canopies, and even indoor spaces [16]. Most LEO-PNT techniques traditionally rely on the deployment of dedicated satellite missions, which can be both costly and resource-intensive. However, an emerging alternative is the use of multiple-input multiple-output (MIMO) beam identification-based methods. These techniques allow for the opportunistic use of existing communication signals transmitted by non-PNT-dedicated LEO satellites, such as those in mega-constellations originally launched for broadband services. By extracting positioning-relevant information from these pre-existing beams, MIMO-based methods can reduce the dependency on dedicated (purpose-built) satellite missions. In other words, each MIMO beam will act as a separate satellite, giving more information on the user's location and reducing the dependencies on launching new satellites. This not only enhances the sustainability of space infrastructure utilization but also promotes a more flexible and adaptive approach to LEO-based positioning. Additionally, this work integrates inertial measurement unit (IMU) data with the LEO beam-based method to improve positioning accuracy and robustness in degraded signal environments. GNSS data is used solely as a baseline for performance comparison, while the fusion approach is focused entirely on LEO-based signals, as further detailed in Section II-E.

In this article, we evaluate and discuss the feasibility of the beam-based positioning method from massive MIMO antennas onboard LEO satellites. The innovation lies within utilizing the beamforming loops incident from MIMO-equipped LEO satellites to provide location information for user terminals (UTs) on Earth. The beam identifiers (ID) and the satellite-to-Earth geometry information are used to obtain estimates of the user position amid the signaling phase of the wireless communications link between the space segment and the user segment. The concept is illustrated in Figure 1, also concretely simulated in a prior research article [17], and further explained in the published patent [18].

The proposed positioning method does not rely on received signal strength (RSS), time offsets, or other traditional physical-layer measurements. Instead, it exploits beam identifiers, making it inherently more tolerant to signal degradations and multipath effects. This characteristic enables it as a promising candidate for robust and low-cost global positioning services with sufficient accuracy for various applications. However, unlike other SoOp-based techniques that extract timing, Doppler shifts, or angle of arrival (AoA) information, the current method does not yet provide timing or clock synchronization.

Recent advances in SoOp positioning have demonstrated real-time AoA estimation using full-digital, reconfigurable receiver architectures synthesized on FPGA platforms [19], [20]. These systems exploit the spatial resolution of MIMO arrays to estimate the position of LEO satellites and, by extension, the user location. While these methods require more complex front-end hardware and signal

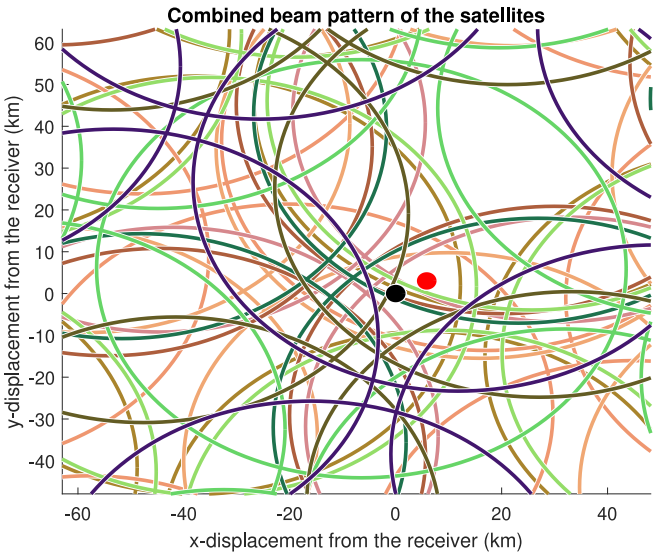

Fig. 1. Illustrating the concept of combined LEO beam footprint patterns. Arbitrary user location estimation (red dot) based on detecting the inbound LEO beam IDs by a user receiver (black dot) actually placed at (0,0).

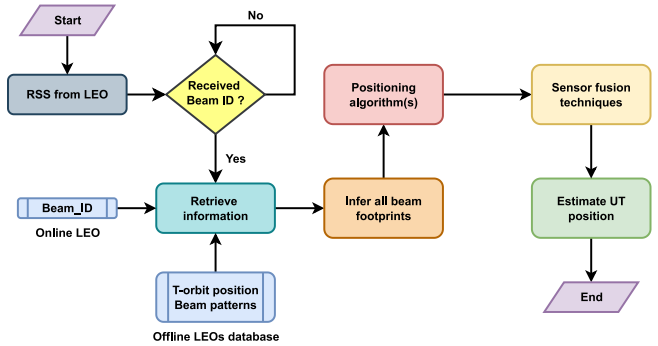

Fig. 2. Stages of the beam ID-based positioning method.

models, they highlight a parallel direction in opportunistic positioning research. Our method complements this line of work by proposing a more lightweight, ID-based approach that prioritizes receiver simplicity and resilience.

The rest of paper is organized as follows: in Section II, we discuss the elements of the proposed beam ID-based positioning concept from technical realization perspective, focusing on its practical implementation and relevance to radio-frequency identification and satellite-based remote sensing. Section III shows how the concept was implemented and evaluated in a simulation test-bed, including key geospatial and signal processing parameters. Section IV contains the rendered results using definitive performance metrics and studying the asymptotic behaviour of error. In Section V, we discuss and comment on the results in addition to the prospects to implement the concept in the future. Finally, Section VI summarizes the findings and predict future work in this area of satellite-based positioning.

II. Methodology

The flowchart of the entire positioning process using beam IDs from MIMO-equipped LEO satellites is illustrated in Figure 2. The method presented in this work can be applied by

both dedicated and opportunistic LEO-PNT systems. As discussed in our preliminary study [21], the satellite beamforming loops are given unique IDs in the downlink super-frames. The beam IDs are used as tokens to fetch the satellite ephemeris (i.e., time stamped position in orbit), satellite orientation, and MIMO beam pattern information from the satellite vehicle (SV). Subsequently, the beams' footprints (coverage area) on Earth are estimated, providing a way to perform user multilateration. This positioning method is not dependent on accurate RSS values, time corrections, or other measurements, but it requires dense satellite constellations. This section proceeds by showing the role of MIMO antennas in LEO satellites to provide a comprehensive overview of the technical aspects of the LEO-MIMO beam ID-based positioning method.

A. MIMO Antennas in LEO Satellites

The mass adoption of MIMO antennas in LEO satellites is still under deployment. Currently, only few to none of the existing satellite constellations are MIMO-capable, but it is expected that one to many of future LEO constellations are to be equipped with MIMO and mMIMO technologies in the following years. This topic has attracted significant research due to its benefits, such as better throughput, higher capacity, and improved quality of service [22].

mMIMO differs from MIMO in terms of the number of onboard antenna elements. mMIMO is implemented by employing 1024 or more antenna elements that are separated by a distance equivalent to half the wavelength [22]. From an opportunistic perspective, both MIMO and mMIMO signals can be exploited to provide location information based on the beamforming loop IDs. When the number of beams increases as in mMIMO, the positioning resolution is expected to be improved.

The congregation of beams from multiple LEO satellites creates a combined footprint pattern that includes numerous intersection regions, even for a single satellite. Increasing the number of satellites and reducing the beam width (via narrower, more focused beams) leads to more localized intersection areas, thus, improving positioning resolution. However, even pencil beams with sub-degree half-power beam widths (HPBW or –3 dB) can result in footprint diameters on the order of tens of kilometers at typical LEO altitudes. This imposes a natural lower bound on the spatial resolution of a single beam-based measurement. Nevertheless, our method does not rely on a single beam but on the unique combination of multiple overlapping beams, each with known geospatial trajectories and time-stamped identifiers. The resulting intersection patterns, when accumulated across several satellites and constellations, can still provide accurate positioning estimates. Additionally, the integration with inertial sensors and post-processing algorithms further refines the output trajectory. The number and geometry of the beams generated by each satellite depend on the specific mMIMO beamforming architecture, which remains a key design parameter for future implementations.

Based on the reviewed literature [23], [24], [25], hybrid beamforming schemes provide flexible control over beam patterns by combining the benefits of both analog and digital beamforming. In this approach, the mMIMO array is divided into sub-arrays, each connected to an RF chain that produces a steerable main beam with a controllable radius.

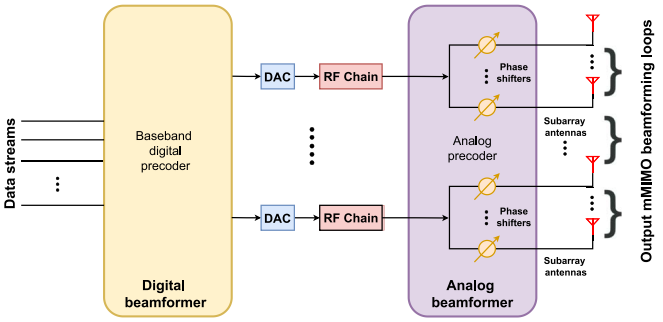

Fig. 3. Block diagram depicting the hybrid beamforming scheme of mMIMO.

While commercial LEO constellations such as Starlink and OneWeb employ advanced beamforming to enable dynamic user connectivity and load balancing [26], [27], they do not publicly disclose the use of beam IDs for positioning purposes. Hence, the beam ID-based positioning approach proposed in this study is considered novel. It introduces an opportunistic use of existing beam infrastructure for navigation, without requiring modifications to the physical signal or dedicated positioning payloads.

For the hybrid beamforming configuration shown in Figure 3, the number of major beams corresponds to the number of allocated RF chains.

B. Beam ID-Based Positioning Method

The proposed positioning method relies on the geometric intersections formed by the congregation of overlapped beams from LEO satellites. This enables position estimation using geometric algorithms. The process in this article consists of two steps: a real-time operation followed by a post-processing algorithm, as detailed in the following sections.

C. Real-Time Positioning Algorithms

For the method to be efficient and viable, the beam patterns of LEO satellites should have known shapes (fixed or variable shapes but known to the users or the positioning engine) and intersect other beams within the same pattern (satellite), like an overlapping mesh shape. Then, whenever the UT receives LEO-mMIMO satellite communications, it should be able to extract each beam's unique ID from the non-payload frame fields. Beam IDs will serve as tokens to fetch more information about the transmitting satellite vehicle, LEO constellation, shape of the beam footprint pattern, timestamped location of the satellite vehicle, and expected beam footprint geographic trajectory on Earth's surface. Eventually, by receiving at least one beam ID from one LEO satellite only, the UT can still infer information about its location on Earth within an error span in kilometers, equivalent to the radius of the received beam footprint.

Upon receiving a LEO satellite signal with a decoded beam ID, the UT starts to search the available dedicated

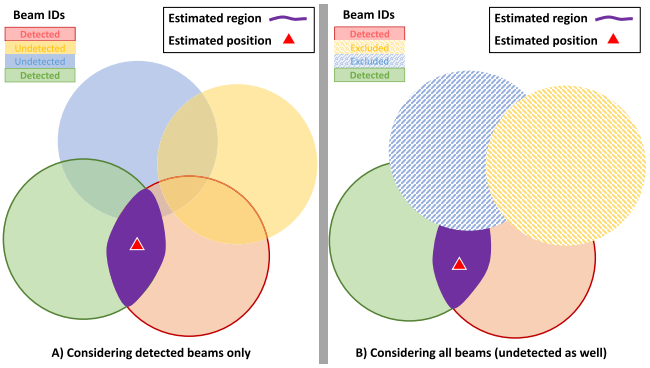

Fig. 4. Two positioning algorithm variants to utilize the information of the beam footprints: (left) ALG. A: The intersection of detected beam footprints defines the possible UT region where the receiver can be located. (right) ALG. B: The position estimate is refined by excluding the regions covered by known undetected beams. These footprints are subtracted from the intersection region defined in ALG. A, resulting in a smaller and more accurate location estimate.

databases for the satellite vehicle carrying this beam, and its live location. The same procedure is done with every other beam ID received by the UT. In the end, the UT shall combine all gathered information from all the received beam IDs in order to pinpoint its position on Earth's coordinates. The chosen way of integrating the positioning information is by assuming that the UT lies at the center of gravity (CoG) of the intersection area of all the detected beams. This procedure is defined as Algorithm A, or "ALG. A", which estimates the user's location using the overlapping beam footprints.

By knowing the whole beam patterns of all received LEO satellites, the information about the absent undetected beams can be included in the calculations to omit their geographical footprints from the beam pattern. This leads to a smaller confined region of intersection than the region resulted from ALG. A, enhancing the mean positioning accuracy, this technique can be called the "B" algorithm or ALG. B. Figure 4 describes both ALG. A and ALG. B with graphical illustration.

ALGs A and B can be defined using mathematical sets and set operations, also known as morphology in image processing. Let $D(t)$ and $U(t)$ be the sets of detected and undetected beam IDs, respectively, for time instant t. Moreover, let $c(i,t)$ be a function that returns the East North (E-N) coordinates of the center of the beam footprint of beam i at time instant t. Similarly, $R(i,t)$ returns the radius of the beam. Mathematical set $A_i(t)$, which includes all locations $\mathbf{x}$ (in E-N coordinates) inside the beam footprint of beam i, can be represented as in Equation (1).

$$A_i(t) = \{\mathbf{x} \mid \|\mathbf{x} - c(i,t)\| < R(i,t)\} \tag{1}$$

Now, intersection $I_A(t)$ for all $\forall A_i(t)$ of the detected beams is a set of E-N coordinates, i.e., an area, where the UT must be located. The intersection is determined by Equation (2).

$$I_A(t) = \bigcap_{i \in D(t)} A_i(t) \tag{2}$$

If the UT was outside the intersection area, it would not detect all the beams in $D(t)$. On the other hand, the UT can be anywhere in $I_A(t)$, and without any additional information

Algorithm 1 ALG. A: Position Estimation via Detected Beam Intersections (Equations (1)–(3))

Require: Set of detected beams $D(t)$ at time t
Ensure: Estimated UT position $\hat{\mathbf{x}}$
1: **for all** $i \in D(t)$ **do**
2: Retrieve beam center $c(i,t)$ and radius $R(i,t)$
3: Define footprint $A_i(t)$ using Equation (1):

$$A_i(t) = \{\mathbf{x} \mid \|\mathbf{x} - c(i,t)\| < R(i,t)\}$$

4: **end for**
5: Compute intersection region using Equation (2):

$$I_A(t) = \bigcap_{i \in D(t)} A_i(t)$$

6: Compute centroid of intersection using Equation (3):

$$\hat{\mathbf{x}} \leftarrow \text{ALG.A}(t) = \frac{\iint_{\mathbf{x} \in I_A(t)} \mathbf{x} \mathrm{d}\mathbf{x}}{\iint_{\mathbf{x} \in I_A(t)} \mathrm{d}\mathbf{x}}$$

7: **return** $\hat{\mathbf{x}}$

(e.g., signal strength or information of the undetected beams) each location $\mathbf{x}$ in $I_A(t)$ is equally probable. Therefore, the ideal point estimate for the position of the UT is the CoG of the intersection region with uniform mass density. This resembles ALG. A, as defined in Equation (3).

$$\text{ALG.A}(t) = \frac{\iint_{\mathbf{x} \in I_A(t)} \mathbf{x} \mathrm{d}\mathbf{x}}{\iint_{\mathbf{x} \in I_A(t)} \mathrm{d}\mathbf{x}}. \tag{3}$$

where integration is done over the entire area of intersection.

The locations of the undetected beams are utilized to shrink the area of possible UT locations. The footprints of the undetected beams can be subtracted from intersection $I_A(t)$ used for ALG. A, as the patterns are supposedly known. The shrunk intersection $I_B(t)$ can be obtained by subtracting the union of the undetected beams from the intersection of the detected beams, as given in Equation (4).

$$I_B(t) = I_A(t) - \bigcup_{i \in U(t)} A_i(t) \tag{4}$$

Finally, the CoG of set $I_B(t)$ is the output of ALG. B, as given in Equation (5).

$$\text{ALG.B}(t) = \frac{\iint_{\mathbf{x} \in I_B(t)} \mathbf{x} \mathrm{d}\mathbf{x}}{\iint_{\mathbf{x} \in I_B(t)} \mathrm{d}\mathbf{x}}. \tag{5}$$

These positioning techniques carried out by the beam ID-based positioning from LEO satellites (i.e., ALG. A, ALG. B) are not sufficiently accurate or reliable for positioning applications. Hence, post-processing algorithms are to be used for more precise positioning results. In addition, a sensor fusion technique is considered to fuse LEO satellite positioning data with an IMU sensor. ALGs A and B are summarized as pseudo-code step-by-step algorithmic format in Algorithms 1 and 2.

Algorithm 2 ALG. B: Refined Estimation via Inclusion/Exclusion (Equations (1), (2), (4), (5))

Require: Sets $D(t)$ and $U(t)$ of detected and undetected beam IDs at time t

Ensure: Estimated UT position $\hat{\mathbf{x}}$

1: **for all** $i \in D(t)$ **do**
2: Retrieve beam center $c(i,t)$ and radius $R(i,t)$
3: Define footprint $A_i(t)$ using Equation (1):

$$A_i(t) = \{\mathbf{x} \mid \|\mathbf{x} - c(i,t)\| < R(i,t)\}$$

4: **end for**
5: Compute detected-beam intersection using Equation (2):

$$I_A(t) = \bigcap_{i \in D(t)} A_i(t)$$

6: **for all** $i \in U(t)$ **do**
7: Retrieve $c(i,t)$ and $R(i,t)$
8: Define $A_i(t)$ using Equation (1):

$$A_i(t) = \{\mathbf{x} \mid \|\mathbf{x} - c(i,t)\| < R(i,t)\}$$

9: **end for**
10: Subtract undetected beam regions using Equation (4):

$$I_B(t) = I_A(t) - \bigcup_{i \in U(t)} A_i(t)$$

11: Compute refined centroid using Equation (5):

$$\hat{\mathbf{x}} \leftarrow \text{ALG.B}(t) = \frac{\iint_{\mathbf{x} \in I_B(t)} \mathbf{x} d\mathbf{x}}{\iint_{\mathbf{x} \in I_B(t)} d\mathbf{x}}$$

12: **return** $\hat{\mathbf{x}}$

D. Post-Processing Algorithms

Since ALG. B (inclusion and exclusion) is more accurate than ALG. A (inclusion only), it will be adopted as the main LEO positioning algorithm throughout the later stages of this implementation study.

The rough estimations carried out by ALG B, are imported to a set of algorithms to further refine the final positioning estimations. Some processing steps are done at the local level (per data source, e.g., at either LEO or IMU) and the global level (sensor data fusion of both LEO/IMU). This strategic approach is undertaken with the primary goal of enhancing the accuracy of positioning estimations, ensuring that the final estimates are more precise and reliable. A bank of algorithms is used to overcome this issue.

In summary, the sequence of algorithmic realization starts with applying ALG. B on the received LEO satellite beam IDs, and whenever a loss of measurements occurs then Dead Reckoning (DR) is activated. Then, the output of the previous steps is fed to a state-space filtering algorithm such as: a Kalman filter and a smoother, which are used to refine the final positioning estimations.

1) Dead Reckoning (DR): in cases of communication loss or data interruptions (due to sensor drifts, signal attenuation or NLOS), the dead reckoning (DR) algorithm can be employed to fill the null posterior state based on non-null prior information. DR is widely used in positioning and navigation applications even before the advent of contemporary localization systems. Equations (6) illustrate DR in mathematical notation.

$$\begin{aligned} D_k &= \sqrt{\left(p^x_{k-2} - p^x_{k-1}\right)^2 + \left(p^y_{k-2} - p^y_{k-1}\right)^2}, \\ \phi_k &= \arctan2\left(\frac{p^y_{k-2} - p^y_{k-1}}{p^x_{k-2} - p^x_{k-1}}\right), \\ p^x_k &= p^x_{k-1} + D_k \cos(\phi_k), \\ p^y_k &= p^y_{k-1} + D_k \sin(\phi_k). \end{aligned} \tag{6}$$

where k is the time instant, p^x_k and p^y_k are the x-y positions, D_k and ϕ_k are the evaluated Euclidean distance and the heading angle, respectively.

2) Extended Kalman Filter (EKF): is a nonlinear state-space estimation technique commonly employed for 2-D and 3-D positioning estimations through conducting two steps: the state prediction step, and the state update step. EKF mathematical procedures [28] are presented in Equations (7).

$$\begin{aligned} m^-_k &= f(m_{k-1}, k-1) \\ P^-_k &= F_x P_{k-1} {F_x}^T + Q_{k-1} \\ V_k &= y_k - h\left(m^-_k, k\right) \\ S_k &= H_x P^-_k {H_x}^T + R_k \\ K_k &= P^-_k {H_x}^T S^{-1}_k \\ m_k &= m^-_k + K_k V_k \\ P_k &= P^-_k - K_k S_k K^T_k \end{aligned} \tag{7}$$

where $m_{\bar{k}}$ and $P_{\bar{k}}$ are the iterative predicted state mean and covariance, respectively, m_k and P_k are the posterior state estimated mean and covariance, respectively. y_k is the input measurements vector, and S_k is the measurement prediction covariance. K_k is the filter gain, $f(.)$ and $h(.)$ are the system dynamic functions of the state-space model and the measurements model, respectively.

The state-space vector $\mathbf{x_k}$ comprises the predicted Cartesian x-y positions, velocities, and accelerations (i.e., a 2-D Wiener dynamic model), while the measurements vector $\mathbf{y_k}$ includes the measurements from LEO satellites (ALG. B). However, the rest of motion kinematics (accelerations and heading angles) are inbound from the IMU sensor, as shown in Equations (8).

$$\begin{aligned} \mathbf{x_k} &= \left[x \ \dot{x} \ \ddot{x} \ y \ \dot{y} \ \ddot{y}\right]^T, \\ \mathbf{y_k} &= \left[x_{LEO} \ \ddot{x}_{IMU} \ y_{LEO} \ \ddot{y}_{IMU}\right]^T. \end{aligned} \tag{8}$$

3) Rauch-Tung-Striebel (RTS) Smoother: is a Bayesian recursive filter that enhances the linearized state-space estimates by retrospectively smoothing the probability density function's maximum likelihood (mean and covariance) [28], [29]. The prior and posterior state estimates $\hat{X}_k|k-1, \hat{X}_k|k$ and their covariances $\hat{P}_k|k-1, \hat{P}_k|k$, which were obtained from the previous filtering (e.g., EKF filtering) are

Algorithm 3 Post-Processing With DR, EKF, and RTS Smoother (Equations (6), (7), (8), (9))

Require: Position estimates $\hat{\mathbf{x}}_k \leftarrow$ ALG.B(t) at each time step k

Ensure: Smoothed UT trajectory

if loss of LEO beam data **then**
  Apply Dead Reckoning using past two positions ▷ Equation (6)
end if
Fuse LEO and IMU data using EKF ▷ Equations (7), (8)
- Predict: $\mathbf{x}_{k|k-1} = f(\mathbf{x}_{k-1})$
- Update: $\mathbf{x}_k = \mathbf{x}_{k|k-1} + K_k(y_k - h(\mathbf{x}_{k|k-1}))$

(State vector and measurement vector structure in Equation (8))

Store filtered states $\{\hat{X}_k|k, P_k|k\}$
Apply RTS Smoother retroactively ▷ Equation (9)
for $k = N-1$ to 0 **do**
  Compute smoother gain C_k
  $\hat{X}_k|n = \hat{X}_k|k + C_k(\hat{X}_{k+1}|n - \hat{X}_{k+1}|k)$
end for
return Smoothed trajectory $\{\hat{X}_k|n\}$

TABLE I
SUMMARY OF VARIABLES USED IN EQUATIONS (1)–(9)

Symbol	Description
$D(t)$	Mathematical set of detected beams at time t
$U(t)$	Mathematical set of undetected beams at time t
$c(i,t)$	E-N coordinates of the ith beam's center at time t
$R(i,t)$	Radius of the ith beam at time t
$A_i(t)$	Mathematical set of all locations inside the ith beam
$I_A(t)$	Area of intersection of detected beams
$I_B(t)$	Area of intersection after considering the undetected beams
k	Time instant
p_k^x , p_k^y	Cartesian x-y positions
D_k	Euclidean distance
ϕ_k	Heading angle
$m_{\bar{k}}$, $P_{\bar{k}}$	Predicted Kalman state mean and covariance, respectively
m_k , P_k	Posterior state estimated mean and covariance, respectively
y_k	Input measurements vector
S_k	Measurement prediction covariance
K_k	Kalman filter gain
$f(.)$, $h(.)$	Dynamics of state and measurements models, respectively
$x, \dot{x}, \ddot{x}$	Position, speed, and acceleration due to x-axis, respectively
$y, \dot{y}, \ddot{y}$	Position, speed, and acceleration due to y-axis, respectively
C_k	RTS smoothing gain matrix
$X_k\|_k$	RTS a-posterior state estimate at time instant k
$X_{k+1}\|_k$	RTS a-priori state estimate at time instant $k+1$

fed to the RTS smoother to calculate the smoothed state estimates $\hat{X}_k|n$ and covariance $\hat{P}_k|n$. The RTS smoother formulas from [28], [29] are described in Equations (9).

$$\hat{X}_k|_n = \hat{X}_k|_k + C_k\Big(\hat{X}_{k+1}|_n - \hat{X}_{k+1}|_k\Big),$$
$$P_k|_n = P_k|_k + C_k\Big(\hat{X}_{k+1}|_n - \hat{X}_{k+1}|_k\Big) \times C_k^T. \tag{9}$$

where $C_k = P_k|_k F_{k+1}^T P_{k+1}^{-1}|_k$, and $X_k|_k$ is the a-posterior state estimate of time instant k and $X_{k+1}|_k$ is the a priori state estimate of time instant $k+1$ which also applies to the covariance.

In this study, the post-processing algorithms employed include: (i) DR, (ii) EKF, and (iii) RTS smoother. The DR algorithm acts as a fallback buffer mechanism during communication failures or data interruptions caused by sensor drift, signal attenuation, or non-line-of-sight (NLOS) conditions, interpolating position estimates based on prior data. The EKF functions as a fusion filter, combining raw LEO positioning estimates from ALG. B with inertial acceleration data from IMU sensor, as formulated in the state-space equations in Equation (8). Finally, the RTS smoother is applied to refine the estimated trajectory by recursively smoothing the EKF output.

Moreover, a simple non-causal moving average filter (window size = 5) was also applied to post-process ALG. B estimates as an alternative approach. This was done to evaluate the necessary level of complexity in post-processing algorithms, as shown in Figure 5.

The post-processing workflow is detailed in Algorithm 3 using a structured pseudocode format.

E. Technical Considerations of Sensor Fusion

Integrating the LEO-MIMO beam-based positioning approach with IMU data significantly enhances both accuracy and robustness [13]. While LEO-based positioning provides extensive coverage and remains functional in GNSS-degraded environments, its short-term precision is limited by satellite geometry and beam configurations. Conversely, IMUs offer continuous, high-frequency motion tracking but are susceptible to drift accumulation over time [30]. By fusing IMU data with the LEO-based method, the IMU mitigates temporary positioning gaps and satellite signal blockages, while the LEO system corrects IMU drift, yielding a more stable and precise positioning solution. This integration is particularly beneficial in urban, indoor, or obstructed environments where consistent accuracy is essential.

At the latest stages of this study, a loosely coupled LEO/IMU integration scheme was implemented to refine the positioning estimates of the beam-based approach. LEO simulation data and IMU measurements were obtained from the Google Smartphone Decimeter Challenge for the 2022 and 2023–2024 episodes [31], [32], referred to as Dataset I and Dataset II, respectively. Additionally, as detailed in Section II-D, an alternative post-processing approach was explored using a simple moving average filter without IMU fusion, to further investigate post-processing algorithm performance.

At the LEO receiver, beam IDs are retrieved from the non-payload frames of the received signal, either during the signaling phase or following the preamble headers. These beam IDs function as tokens to access the LEO satellite ephemeris and beam pattern shapes from the connected data server. Subsequently, positioning estimation is performed using ALG.B, providing an initial location prediction within Earth's coordinate system. Post-processing is then conducted through one of two methods: either via 1) EKF and RTS smoothing with IMU fusion or 2) through a smoothing moving average without fusion. Figure 5 presents the framework of futuristic LEO-based handheld receivers, which are designed to utilize this beam-based positioning methodology along with sensor fusion schemes.

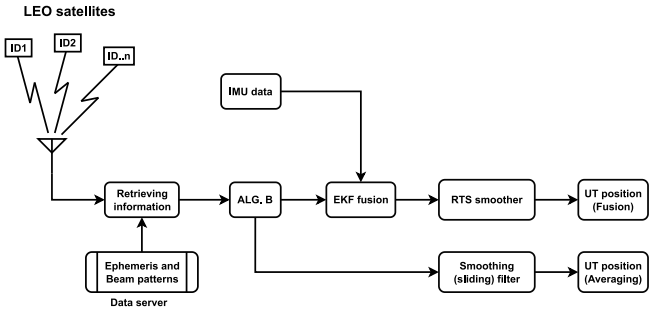

Fig. 5. Block diagram of the proposed LEO-MIMO based receiver.

III. Simulation Setup

The objective of the simulation is to reproduce beam ID-based positioning method and evaluate its accuracy with future mega constellations of LEO satellites. In the simulation, both UTs and the satellites move with a temporal resolution of 1 second. The total simulation time is 1,200 seconds, i.e., 20 minutes.

The simulation has been developed with the following characteristics, simplifications, and presumptions: i) There are several LEO mega constellations that are launched in a grwoing sequence. Thus, it is possible to analyze how the accuracy of the positioning method evolves as new constellations with more advanced beamforming capabilities are introduced. ii) The positions of the satellites relative to the UT are calculated using a local planar coordinate system. iii) Each beam has a circular *footprint* on Earth (more specifically, on the plane around the UT), despite varying elevation angles. iv) If the UT is inside a beam footprint, it recognizes the beam ID with a 100% probability. If the UT is outside a beam footprint, it recognizes the beam ID with a 0% probability. v) The UT can read all available beam IDs simultaneously within the same coverage area.

A. Simulating Beam Footprint Patterns

We assume that a LEO satellite transmits several beams that form a regular beam footprint pattern on Earth. For every satellite of a specific satellite constellation, all beams have identical radii, R, and the centers of the adjacent beam footprints are separated by $1.5R$, i.e., the adjacent beams partially overlap. Different constellations have different beam footprint radius. When several satellites transmit their beams at the same time, the beam footprint patterns overlap. A schematic example (with a reduced number of beams for clarity) of a combined beam footprint pattern is shown in Figure 6.

Based on the illustration shown in Figure 7, the coverage area of a single LEO satellite can be evaluated from Equations (10), and (11). Then, the coverage area is divided into smaller beamforming loops according to Equation (12).

First, the coverage geometry is approximated to the relation in [33, Eq. (10)].

$$cos(\theta + \epsilon) = \frac{cos(\epsilon)}{1 + \frac{h}{R_E}} \tag{10}$$

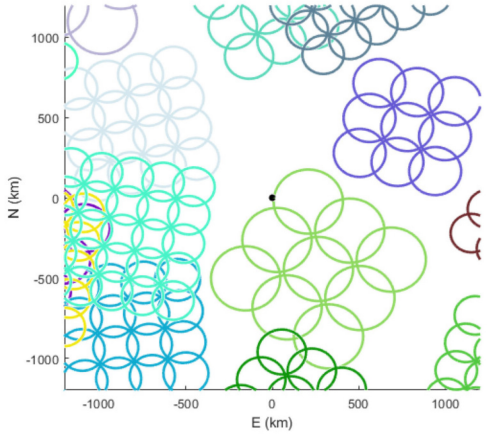

Fig. 6. Randomly selected beam footprint patterns from constellations 1-5 (see Table III for the beam pattern parameters of corresponding constellations).

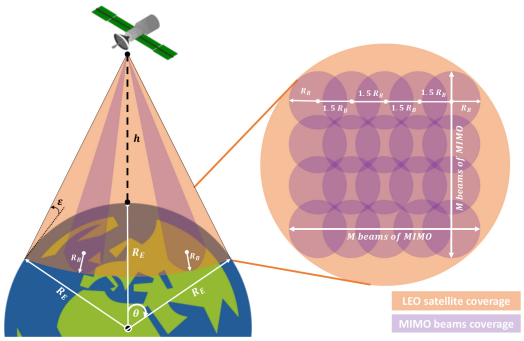

Fig. 7. Coverage area of a single LEO satellite with MIMO beams.

whereas θ is the central conic angle in radians measured from Earth's center, ϵ is the elevation angle of the viewing cone of the satellite, h is the altitude of the LEO satellite, and R_E is Earth's radius.

Considering higher and moderate elevation angles (e.g., $45° \leq \epsilon \leq 135°$), therefore, the coverage area A can be evaluated approximately from Equation (11). In which, the shape of the LEO satellite coverage area is approximated to be equivalent to the shape of a spherical cap [34], enclosing θ as the central angle.

$$A = 2\pi R_E^2 (1 - cos(\theta)) \tag{11}$$

where θ is the central angle, and A is the coverage area approximated as a spherical cap shape.

Afterwards, for MIMO implementation considering Figure 7, the radii of beamforming loops can be approximately determined from the evaluated LEO satellite coverage area as in Equation (12).

$$A \approx (2R_B + (M - 1) \times 1.5R_B)^2 \tag{12}$$

where A is the coverage area, R_B is the beam radius, and M is the squared size of MIMO ($M \times M$).

B. Satellite Mega Constellations

The satellite mega constellations were reproduced with an in-house simulator tool, named LEO-S9 (LEO simulator with

TABLE II
STATUS AND ORBIT PARAMETERS OF THE CURRENT AND PLANNED LEO CONSTELLATIONS. VALUES BASED ON [36]

Mission	Altitude [km]	Inclination [°]	N. Sats.
OrbComm	740 - 875	45, 70, 72	47
Globalstar	1400	52	48
Iridium	625, 720	86	66
Telesat	1015, 1325	51, 98	1671
Kuiper	590 - 630	33, 42, 52	3236
OneWeb	1200	40, 55, 88	6372
Starlink	540 - 570	53, 70, 98	$>$ 10000

9 modules) [35]. The LEO-S9 tool is flexible to create a variety of space segment scenarios, including diverse dynamics and instruments specific to LEO satellites. The main relevant data attributes simulated with LEO-S9 in this work included the orbit altitude, inclination, velocity, constellation topology, and initial design. The constellation progress with time was reproduced considering the Cowell numerical integration, Earth's gravity, J_2 oblateness effect, third body attractions, solar radiation, and atmospheric drags. A walker delta topology was selected to keep a symmetric coverage.

The simulation was built by considering the present status and upcoming developments in LEO satellite missions. Table II provides an overview of the primary missions and associated orbit parameters that were considered in this study, and the generation of LEO satellite constellation data.

To assess the performance of the proposed method across various LEO coverage scenarios, simulations for 13 distinct case scenarios were conducted, each denoted as experimental cases 1 through 13. In the initial case, 3000 satellites were simulated, covering a diverse combination of all identified missions. Then, about $\sim$1000 additional satellites were incrementally included into the simulation for each subsequent case. Notably, experimental case 13 assumed the operation of a total of $\sim$15000 LEO satellites. Meaning that every constellation of the 13 generated scenarios is enough to cover the most populated areas of Earth. While this may seem ambitious, it is a foreseeable scenario in the forthcoming years. On the other hand, the test case scenarios are numbered 1–4, to cover three modes of motion: stationary, linear, and nonlinear motion.

The parameters of the generated LEO satellite constellations (number of satellites, number of beams per satellite, the radii of the beams, and the spacial separation of the beams) for motion Scenarios 1–3 are given in Table III. The adjacent beams centers were separated by ($1.5 \times R_{\text{beam}}$) for all constellations, satellites, and beams. This separation value was set in order to impose large-sized beam intersections needed for the beam ID-based positioning method to have sufficient overlapping of beam congregations within both the satellite and the whole constellation. Whereas, the increased overlapping incidents from more beams shall result in better accuracy.

C. Simulation Scenarios

Three use case setups were simulated: 1) stationary UT, 2) UT in slow uniform linear motion, 3) UT moving through a pre-defined route. For each use case, several simulations experiments were performed in order to evaluate the accuracy of the positioning method and algorithms when using realistic future satellite mega constellations with MIMO capabilities and later with mMIMO configurations. Each experiment consisted of several simulation runs with changing parameters depending on the objective of the experiment. The rotation angles of the beam footprints were randomized for each simulation run but kept constant during the ongoing run.

TABLE III
LEO SATELLITE CONFIGURATIONS FOR SCENARIOS 1–3

Const.	Sats.	Beams/sat.	R_{beam}
1	3000	3×3	200 km
2	4050	3×3	150 km
3	5040	3×3	140 km
4	6048	4×4	130 km
5	7020	5×5	120 km
6	7992	6×6	110 km
7	9012	7×7	100 km
8	10002	8×8	90 km
9	11052	8×8	80 km
10	12072	8×8	70 km
11	13032	8×8	60 km
12	14004	8×8	50 km
13	15084	8×8	40 km

Each simulation run is generated with the following data fields: true position in (E, N), estimated position by ALG. A in (E, N), estimated position by ALG. B in (E, N), positioning error, number of detected beams. The parameters of the satellite constellations (number of satellites, number of beams per satellite, the radii of the beams, and the spacial separation of the beams) are given in Table III. The adjacent beams centers are separated by $1.5 \times R_{\text{beam}}$ for all constellations, satellites, and beams; in order to increase the beam intersections.

The user scenarios are described as follows:

1) Variation of Error Metrics: : The objective of the first experiment is to evaluate the confidence intervals of the error metrics. It is done by measuring the standard deviation of the error metrics while varying the location of the user terminal. The primary measurement is the sensitivity of the positioning error to the location of the user terminal. Because the simulation model is heavy to compute, the confidence intervals are evaluated separately for one set of simulation parameters, in contrast to repeating each experiment several times to obtain their standard deviation estimates individually.

2) Use Case Scenario 1—Stationary User Terminal: When the user terminal does not move, it is possible to collect samples from the probability distribution of the true position. As LEO satellites move fast, the beam footprint pattern changes rapidly. Therefore, sampling positions with a 1 Hz rate is expected to give a time series without auto-correlation. If the positioning estimates are unbiased and uncorrelated, the mean value of the samples will converge towards the true position. This will be investigated experimentally using convergence time spans from 1 to 30 seconds.

3) Use Case Scenario 2—Slow Uniform Linear Motion: In Scenario 2, the user terminal moves with a constant speed of 1 m/s towards North-East. The initial position is at (latitude, longitude) = (37.773972, -122.431297), i.e., in

TABLE IV
LEO SATELLITE CONFIGURATIONS OF SCENARIO 4

Const.	Sats.	Beams/sat.	R_{beam}
1	3000	64×64	20 km
2	4050	64×64	19 km
3	5040	64×64	18 km
4	6048	64×64	17 km
5	7020	64×64	16 km
6	7992	64×64	15 km
7	9012	64×64	14 km
8	10002	64×64	13 km
9	11052	64×64	12 km
10	12072	64×64	11 km
11	13032	64×64	10 km
12	14004	64×64	9 km
13	15084	64×64	8 km

San Francisco, California. This Scenario corresponds, e.g., to a person walking or an autonomous vehicle driving slowly along a straight street. As the movement is easy to predict, it is presumed that the post-processing methods converge effectively towards the correct location.

The procedure is similar to Scenario 1, except that the location of the user terminal is not fixed but a time series of 1,200 values and it is not meaningful to apply a sliding average filter to the time series of the estimated positions.

4) Use Case Scenario 3—Realistic Nonlinear Motion: In Scenario 3, the user terminal moves along the predefined route is located in San Francisco, California. The data is from Google GNSS competition 2022 [31]. For this dataset we also have IMU data that can be used for sensor fusion tests. Scenario 3 is used to evaluate our positioning method in a use case of realistic nonlinear movement, including periods of acceleration, deceleration, change of direction, as well as immobility.

5) Use Case Scenario 4: Real Nonlinear Motion With mMIMO: This Scenario was the repetition and reproduction of Scenario 3 but with mMIMO elements equipped in LEO satellite constellations. In which, the same LEO constellation sizes were used (i.e., 13 constellations with the defined number of satellites per constellation in Table III), however, the number of beams per satellite and the radii of the beams were changed to mMIMO beam configurations.

Scenario 4 was developed to utilize the maximum available resources of LEO satellite constellations and mMIMO beamforming sizes. In which, the 13 constellations were used to provide 64×64 beams from each of the 117,408 LEO satellites. Hence, the beam radii were computed following Equation (12), as given in Table IV.

To summarize the scenarios in a nutshell:

- Scenario 1: a stationary user – MIMO
- Scenario 2: a uniformly moving user – MIMO
- Scenario 3: a real nonlinear motion of a user – MIMO
- Scenario 4: a real nonlinear motion of a user – mMIMO

D. Drive Test Datasets

For the stationary and uniform motion scenarios 1–2, test datasets were generated using Gaussian probability distribution functions for a fixed location in Scenario 1, and uniformly moving user in Scenario 2.

TABLE V
VARIATION OF ERROR METRICS: SAMPLE MEAN ± STANDARD DEVIATION FOR MAE, RMSE AND MAXIMUM ERROR (MAX) IN KM

Alg.	Const.	MAE	RMSE	MAX
A	3	14.0 ± 0.52	16.8 ± 0.63	55.65 ± 5.70
A	5	4.71 ± 0.14	5.80 ± 0.18	23.67 ± 3.10
B	3	7.55 ± 0.26	9.15 ± 0.37	34.52 ± 5.49
B	5	2.38 ± 0.08	2.91 ± 0.10	12.32 ± 1.86

For the real nonlinear motion scenarios 3–4, Google decimeter challenge datasets from 2022 and 2024 were used [31], [32] as drive test data. Scenario 3 emulated parts of the drive test data from [31], and Scenario 4 emulated parts of the drive test data from both [31] and [32]. Scenario 4 is the only scenario that was tested on two different real datasets for validation, they are referred to as dataset I from [31], and dataset II from [32], respectively.

E. Limitations

The current simulation setup assumes idealized binary beam ID detection, where reception is perfect inside the beam footprint and absent outside. This simplification enables a clear evaluation baseline but omits real-world effects such as multipath propagation, shadowing, and partial beam edge coverage. Future work should consider probabilistic beam detection models and incorporate signal quality metrics to better reflect urban and obstructed environments.

Additionally, Doppler effects due to the rapid motion of LEO satellites were not explicitly modeled. Since the proposed beam ID-based positioning method relies solely on the successful detection of compact identifier messages, rather than full signal demodulation or Doppler-based ranging. Such effects were considered secondary for this study. However, Doppler shifts may influence detection thresholds and acquisition times in real-world receivers, hence, future implementations should incorporate Doppler compensation strategies accordingly.

IV. RESULTS

In this section we present and evaluate the output results of all three scenarios: the stationary position, the uniform linear motion, and the real vehicle drive test.

A. Variation of Error Metrics

Table V gives the sample means and standard deviations of error metrics with three and five mega constellations, for ALGs A and B. Standard deviations estimate the sensitivity of the error metrics with respect to the UT location. They are used to estimate the error margins of the results. It can be concluded that the relative standard deviation of MAE and RMSE is about 3-4% and the relative standard deviation of the maximum error is about 10-16%.

Figure 8 illustrates the relationship between the number of LEO constellations and the resulting positioning error in kilometers using ALG.B of the proposed beam ID-based method. The results demonstrate an exponentially decaying

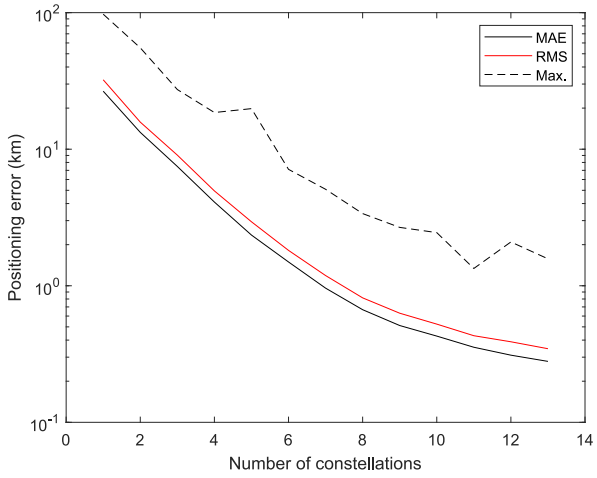

Fig. 8. Positioning error in Km versus number of constellations for ALG. B.

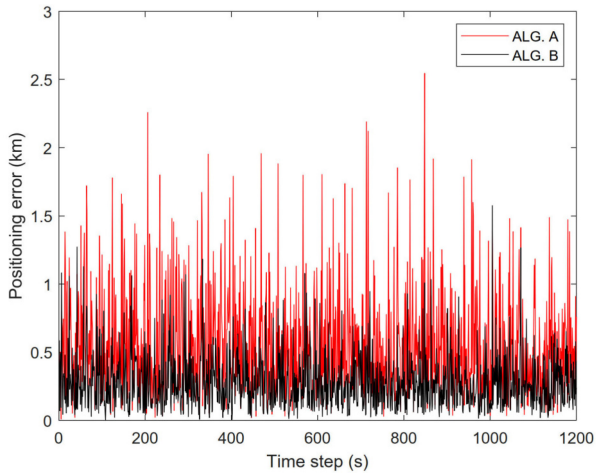

Fig. 9. Positioning error vs. time with 13 constellations.

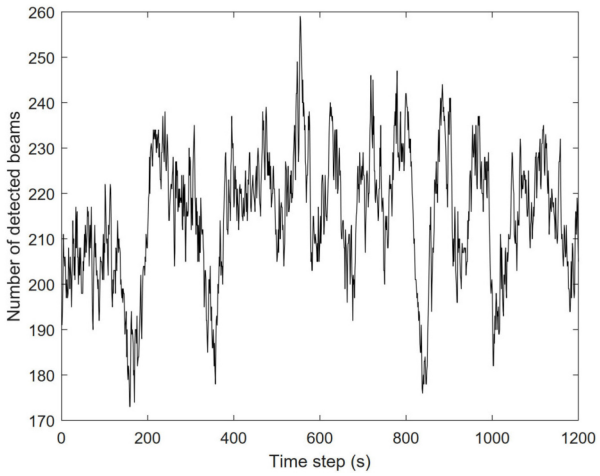

Fig. 10. Number of detected beams over time with 13 constellations.

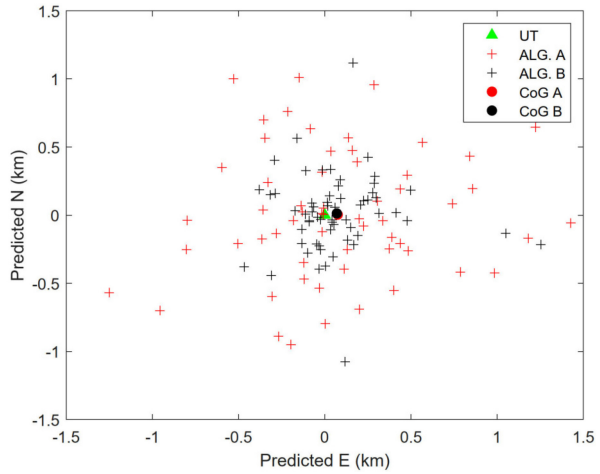

Fig. 11. Scatter plot of position estimates (N=60) using 13 constellations.

trend, where increasing the number of constellations significantly improves accuracy, as expected. Notably, even with a limited number of constellations (e.g., 4–6), the method still achieves sub-kilometer-level accuracy, indicating that practical deployment is feasible even without relying on extremely large-scale LEO infrastructures. This analysis confirms that while larger constellations offer higher precision, an acceptable performance can still be achieved under more conservative and realistic satellite deployments.

B. Use Case Scenario 1: Stationary User Terminal

Figures 9 and 10 show raw time series of positioning errors (for ALGs A and B) and the number of detected beams (identical for ALGs A and B), respectively. These demonstrate the amount of variation when the satellites move during a time span of 20 minutes.

Figure 11 shows how the 60 first samples of the time series of the estimated positions are scattered around the UT. It can also be seen that the two-dimensional mean values (CoG, center of gravity) of the estimated positions are close to the true position of the UT, which indicates that ALGs A and B give unbiased position estimates. Therefore, it is possible to use several samples and averaging to obtain more accurate position estimates, in case of a stationary UT.

The results show that the RMS positioning error decreases when increasing the length of the sliding averaging filter. Based on the central limit theorem and the presumption of independent and identically distributed position estimates, we further assume that the reduction of the RMS error is inversely proportional to the square-root of the window length, as shown in Relation (13).

$$RMSE \propto \frac{1}{\sqrt{w}} \tag{13}$$

where w = window length of sliding average filter.

Based on the graphical and numerical representations of the results, the inverse square-root law holds rather accurately when the number of satellites is very large. Thus, the law is applicable when extrapolating positioning errors for longer convergence periods.

The results show that ALG. B gives more accurate position estimates than ALG. A. However, this holds only for the average accuracy as shown in Figure 9. It demonstrates that ALG. B actually gives quite often better position estimates.

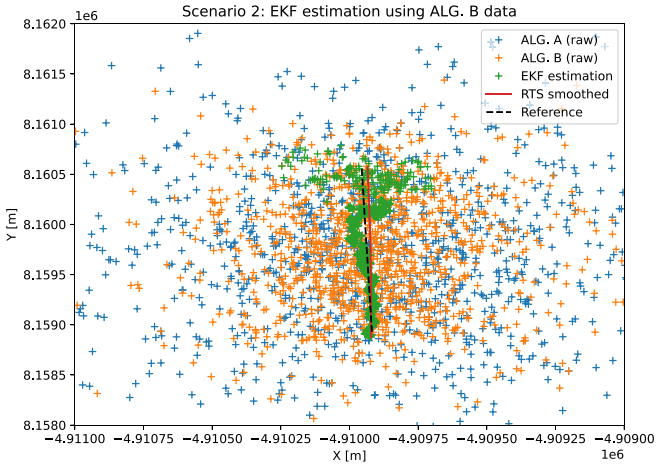

Fig. 12. Scenario 2: EKF and RTS positioning estimations of a uniform linear motion using ALG. B.

TABLE VI
ERROR EVALUATION OF LINEAR MOTION (SCENARIO 2)

Method	Const.	MAE [m]	RMSE [m]	p95% [m]
ALG. A	13	508.49	685.91	1179.1
ALG. B	13	241.61	334.28	588.10
EKF	13	47.25	75.02	982.20
EKF-RTS	13	13.69	15.24	993.86

The probability that ALG. B gives more accurate estimates than ALG. A is 24.2% in this case. In the future, it should be studied if it is possible to utilize the estimates of both algorithms, together with other information, to obtain more accurate position estimates.

The more beams there are congested near the UT, the more accurate positioning is, when keeping other things, such as the size of the beams, unchanged. The number of beams that an UT detects on average (on an arbitrary place on Earth) can be calculated theoretically. It is the ratio of the total area of all beam footprints of available constellations with the area of Earth (510,100,000 km^2). It can be noted that the average value of simulation is well aligned with the theoretical value. It also shows how the number of detected beams increases when adding new constellations to the simulation, according to our mega-constellation model given in Section III.

Finally, from 117,408 LEO satellites and 5,908,000 beams, the UT detects 215 beams on average. The MAE accuracy of Scenario 1 = 0.29 km, the RMSE = 0.35 km, and the maximum error = 1.6 km. When averaging 30 measurements, MAE = 0.057 km, RMSE = 0.064 km, and maximum error = 0.152 km.

C. Use Case Scenario 2: Slow Uniform Linear Motion

The results of Scenario 2 as found in Figure 12 and Table VI show very fluctuating raw position estimates in comparison to the straight imaginary route that resembles a person walking in a uniform speed of 1 m/s. Fortunately, the EKF filtering has reduced the positioning error by approximately 80%, and the RTS smoother has further eliminated around 73% of the EKF output error to achieve an overall accuracy of 16.69 meters as MAE. The 95-percentile value of 993 meters

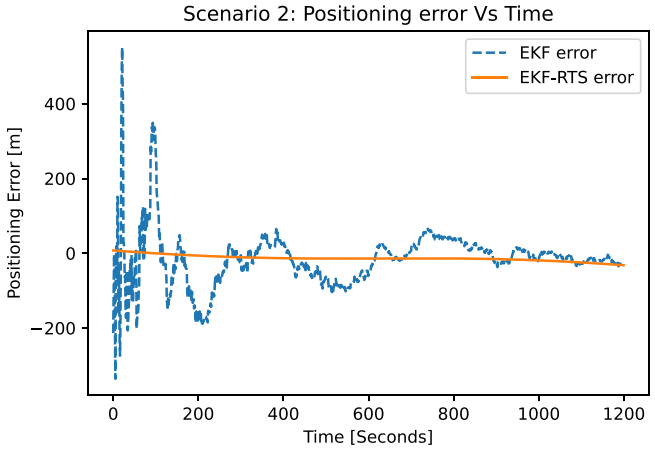

Fig. 13. EKF and RTS error convergence over time in Scenario 2.

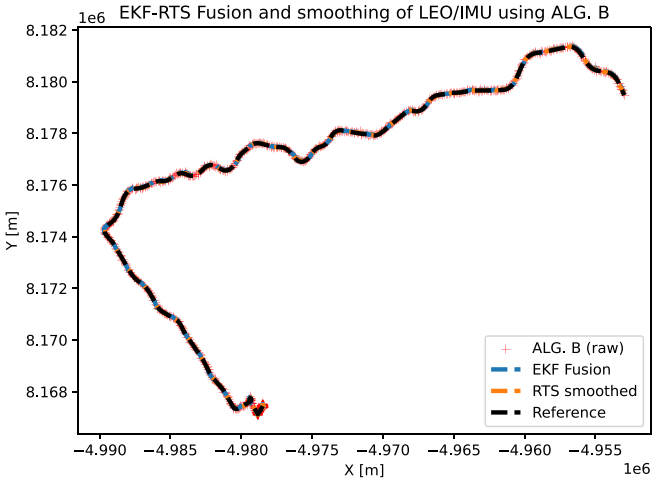

Fig. 14. LEO/IMU fusion using EKF and EKF-RTS on ALG. B data in x-y coordinates.

is large, but it is mostly due to the first output samples of the filters. According to Figures 12 and 13, the position estimations gradually converge towards the true location of the UT. It is unclear why the EKF outputs fluctuate heavily. Notably, during our investigations we found that a simple sliding average filter (window length, $w = 100$) outperforms EKF in smoothing the outputs of ALG. B estimations. Thus, it signifies the potential to improve the accuracy in the future.

D. Use Case Scenario 3: Realistic Nonlinear Motion

The results of Scenario 3 are very promising and satisfactory, as shown in Figures 14, 15, 16, 17, and Table VII.

Primarily, it is clear from trajectory Figures 14 and 16 that the combined EKF-RTS fusion-smoother back-to-back algorithm (using ALG. B) is the most accurate method that is closely following with the ground truth and GNSS with minimal errors. Hence, the applied elementary positioning algorithms after receiving beam IDs (i.e., ALG. A and ALG. B) are not sufficient for conducting a reliable satellite-based positioning on their own, rather, they constantly require a set of post-processing algorithm, similar to every other positioning technologies, e.g., in GNSS.

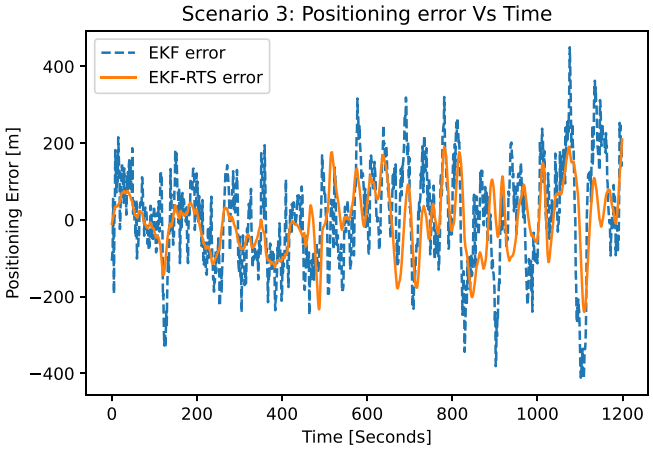

Fig. 15. EKF and RTS error convergence over time in Scenario 3.

TABLE VII
ERROR EVALUATION OF MIMO METHODS VS. GNSS IN SCENARIO 3

Method	Const.	MAE [m]	RMSE [m]	p95% [m]
ALG. A	13	498.16	683.49	1179.5
ALG. B	13	231.59	317.95	520.06
LEO/IMU EKF	13	104.80	132.00	203.35
LEO/IMU EKF-RTS	13	66.31	83.98	142.39
GNSS only	N/A	26.63	36.42	56.60

The numerical positioning error values in Table VII and the error plots illustrated in Figure 15 are confirming the same finding; that the EKF-RTS method outperforms all other algorithms used in this simulation. The CDF curves in Figure 17 imply that the final LEO/IMU positioning estimations are very close to the performance of GNSS in terms of accuracy and precision. However, it is evident that the best performance of LEO/IMU that can match GNSS performance is only achievable using the growing numbers of satellites and constellations, which are 13 constellations carrying more than 100,000 satellites.

In fact, the simulation of Scenario 3 confirms the early hypothesis in this study; that is the necessity of receiving the maximum available interconnected LEO satellite beams in order to improve the final positioning estimations. The number of received beams in Scenario 3 fluctuated between 172 and 247 beams, with average number of detected beams = 214.

E. Use Case Scenario 4: Realistic Nonlinear Motion With mMIMO

This scenario was tested on two distinct datasets: dataset I and dataset II, as stated in Section III-D.

For dataset I results, Figure 18 and the left-hand side of Figure 19 demonstrate the error behaviour of Scenario 4, along with a graphical illustration of its route on the map. While in Table VIII, the positioning errors were investigated using MAE, RMSE and p95% metrics to assess all steps of the fusion based methods of LEO/IMU EKF-RTS. However in a conjugate version of Scenario 4, a simple moving average filter was used to filter the raw ALG. B and show its effect. The best result was found to be with the sliding averaging of the unprocessed ALG.B estimations, as found in Table VIII.

TABLE VIII
ERROR EVALUATION OF MMIMO METHODS VS. GNSS IN SCENARIO 4-I

Method	Const.	MAE [m]	RMSE [m]	p95% [m]
Raw ALG. B data	13	19.27	25.74	44.32
LEO/IMU EKF-RTS	13	9.90	12.71	20.97
Smoothed ALG. B	13	9.15	11.94	19.07
GNSS only	N/A	26.63	36.42	56.60

TABLE IX
ERROR EVALUATION OF MMIMO METHODS VS. GNSS IN SCENARIO 4-II

Method	Const.	MAE [m]	RMSE [m]	p95 [m]%
Raw ALG. B data	13	19.36	27.11	43.46
LEO/IMU EKF-RTS	13	9.47	12.44	21.40
Smoothed ALG. B	13	9.42	12.05	21.18
GNSS only	N/A	18.55	22.24	36.38

From Figures 18 and 19, clearer views of assessment can be found, graphically. Where the LEO/IMU EKF-RTS fusion-based method of Scenario 4 applied on dataset I matched the accuracy of the smoothed unprocessed ALG.B measurements, and both methods outperformed GNSS accuracy.

For dataset II results, Figures 19 and 20 demonstrate the error behaviour of Scenario 4–II, along with a graphical illustration of its route on the map.

In Table IX, the positioning errors were investigated using MAE, RMSE and p95% metrics to assess all steps of the fusion based methods of LEO/IMU EKF-RTS in Scenario 4 applied on dataset II.

Once again, the LEO/IMU EKF-RTS fusion-based method of Scenario 4–II already closely matched the accuracy of the smoothed unprocessed ALG.B measurements, and both methods outperformed GNSS accuracy.

V. DISCUSSION

The simulation was executed using the in-house LEO-S9 simulator in MATLAB environment, in addition to Python scripts for the post-processing algorithms, with 1-second resolution over 1,200 seconds. The raw beam-ID method can produce a first location estimate after a single timestamp when at least one beam is detected, resulting in a theoretical time-to-first-fix (TTFF) of approximately 1 second. However, for the LEO/IMU fusion case in Scenario 2, the positioning error was observed to converge to a stable and accurate range after roughly 180 seconds. This convergence duration reflects the behavior of the EKF smoothing filter in dynamic conditions.

The efficiency of the beam ID-based method is dependent on LEO satellites mega constellations equipped with mMIMO capabilities. Accuracy of initial measurements (i.e., raw ALG. A or ALG. B) is in the order of kilometers when having a few thousands of LEO satellites. When the number of satellites exceeds a hundred thousand, positioning errors of hundreds of meters can be achieved. Positioning with such errors can be used as back-up method, e.g., in aviation, seafaring, situational awareness, search and rescue missions. However, our experiments showed that by the integration (fusion) with other measurements sensors (e.g., IMU), the positioning accuracy can be improved significantly. MAE as small as 14 meters was recorded for a slow uniform linear motion (Scenario 2) when using 13 mega constellations. With

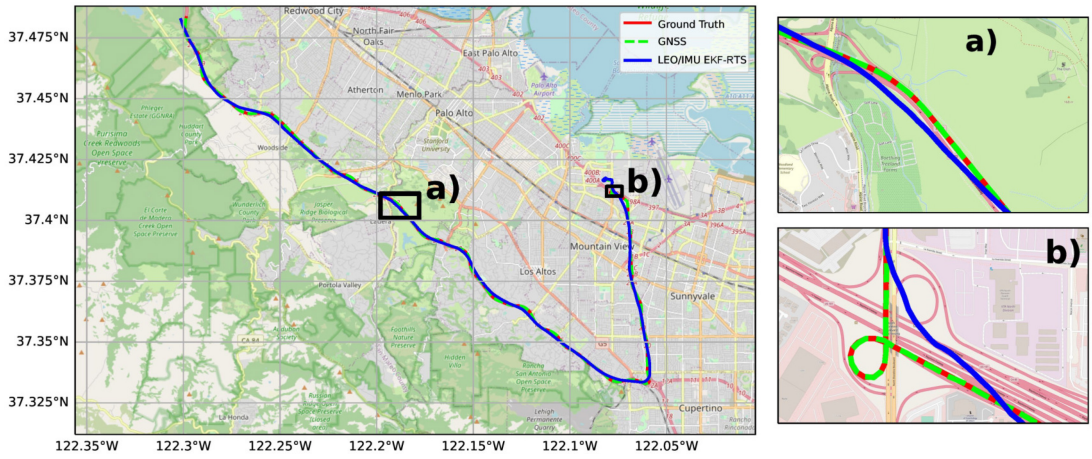

Fig. 16. Map trajectory of Scenario 3: MIMO and GNSS routes in California, USA. The dataset is a courtesy of Google decimeter challenge 2022.

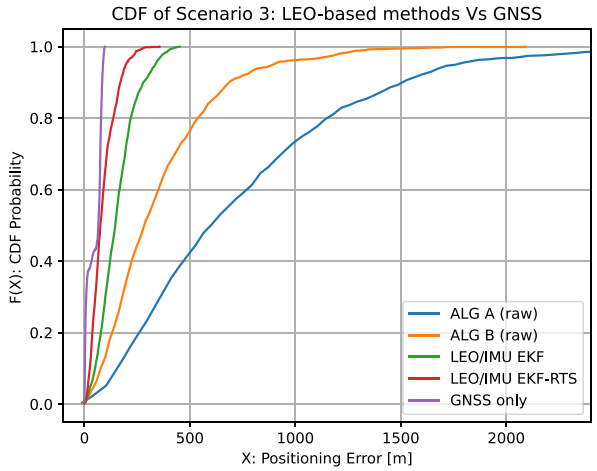

Fig. 17. Cumulative distribution functions of MIMO methods Vs. GNSS.

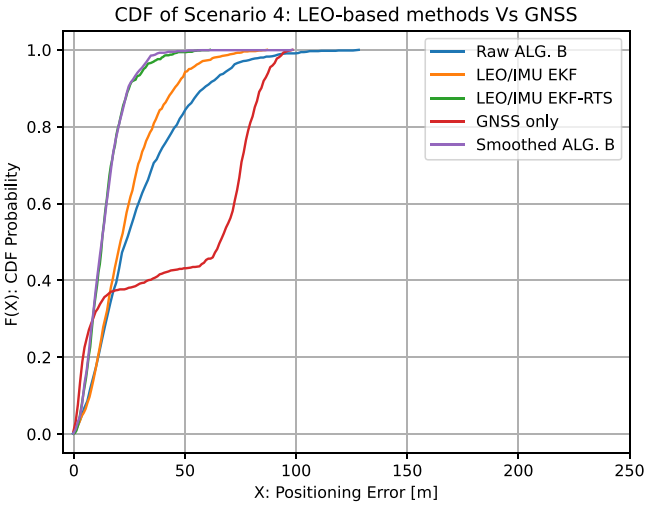

Fig. 18. Cumulative distribution functions of mMIMO methods (I) Vs. GNSS.

advanced post-processing algorithms, an accuracy closer to GNSS systems' is possible. In Scenario 3, with a realistic nonlinear motion, both RMSE metrics for LEO/IMU EKF-RTS and for GNSS were approximately 84 m and 36 m, respectively, and MAEs were approximately 66 m and 27 m, respectively. Meaning that, the beam ID-based positioning method is a promising candidate even for nonlinear dynamic motion of vehicles.

Finally, the results of Scenario 4 are very promising since all its denominations were performing better than GNSS in the event of implementing LEO/IMU fusion. The effect of introducing mMIMO can be seen through the error shift from Figure 17 to Figure 19, where the enhancement in accuracy was significantly proven. By increasing the size of LEO satellite constellations to be 'mega-size' and incrementing the size of regular MIMO beamforming loops to be 'massive', the positioning accuracy can be significantly enhanced to a precise-accurate level of performance. The fusion-based positioning schemes are still effective with LEO satellites, however, even in the event of no multisensor fusion integration, the proposed method can still perform quite well with raw measurements.

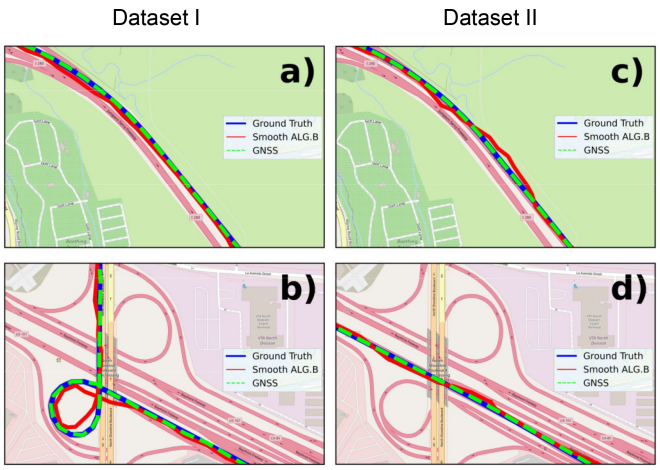

Fig. 19. Routes of datasets I and II in Scenario 4 with LEO positioning results compared to GNSS. Same arbitrary locations were retrieved for comparison.

There are possibilities to further improve the accuracy of the beam ID-based positioning method. Presuming that the signal strength of the beam footprints decreases from the beam center

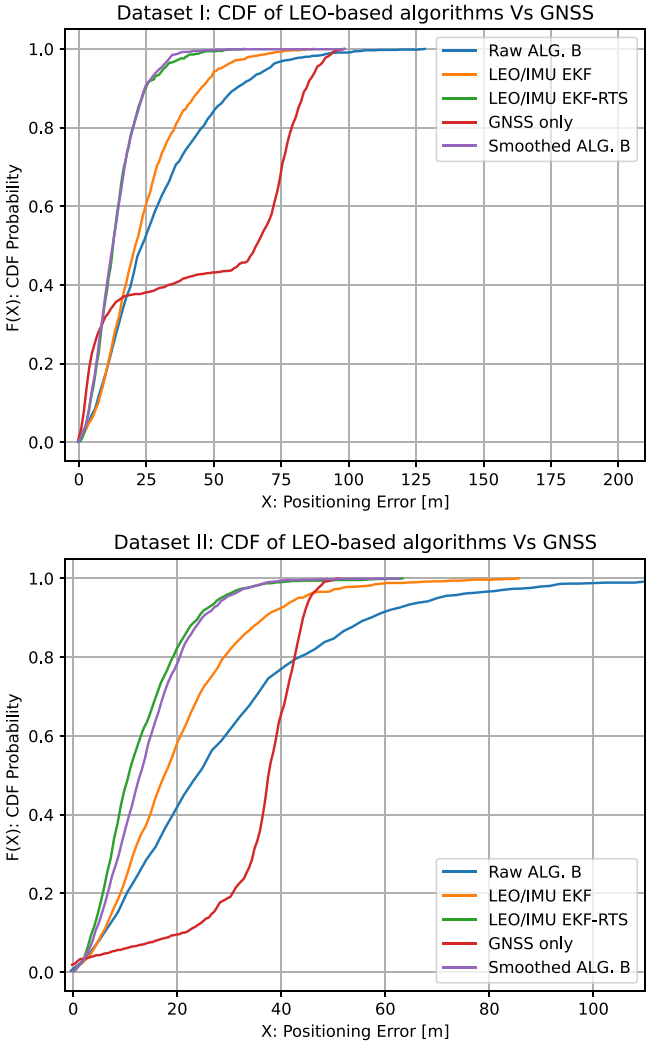

Fig. 20. CDF plots of the used algorithms in both datasets I and II.

towards its borders (in a predictable way), it could be measured and used as an additional weighed input. Similarly, other signal quality metrics could be utilized such as: signal-to-noise ratios. In the post-processing phase, the number of detected satellites could be used to weigh the raw measurements. This is based on the presumption that the more satellites are detected, the more accurate the position estimate becomes, on average.

The beam ID-based position method has several advantages for sustainability. First, it uses measurements that do not require precise timing or accurate measurements of the signal strength. Therefore, the required technology at the user segment is expected to be affordable, which promotes social sustainability. Second, the method does not require dedicated satellites to work. This should reduce costs further and save both energy and natural resources. Third, due to the high signal strength of the LEO satellites and the simple binary measurements (beam is either detected 100% or not 0%) the method is expected to be tolerant towards interference and jamming, especially when fused with the IMU sensor that itself is tolerant to interference as a passive sensor. Hence, the method could guarantee uninterrupted positioning services, also in conflict areas. This has several consequences to sustainable development through the uninterrupted operation of numerous autonomous systems that will promote sustainable development in the future.

From a practical standpoint, the feasibility of a receiver capable of acquiring approximately ∼200 beams per second across multiple LEO constellations is a valid concern. However, it is important to note that the proposed beam ID-based method does not require full signal demodulation; rather, it only relies on the detection of beam identifiers, which are compact binary messages. Since each beam identifier is a compact binary message that includes minimal metadata and a timestamp, the overall bandwidth required to process hundreds of beams per second remains relatively low and well within the capacity of standard low-rate communication channels. Such identifiers are analogous to distress or beacon packets commonly used in satellites, typically under 144 bits and transmitted over narrowband channels (∼3 kHz) [37], [38], [39], indicating that even processing hundreds of beam IDs per second would consume only a minor share of the available bandwidth, for instance, well below 5 kbps. This modest bandwidth can be handled by even low-data-rate telemetry channels. Regarding the hardware architecture, simultaneous acquisition over all 13 constellations does not necessarily demand 13 dedicated radio front-ends. With recent advances in software-defined radio and wideband RF front-end designs, it is feasible to time-multiplex between constellations or the use of configurable multi-band receivers. Moreover, adaptive constellation selection can be employed depending on satellite visibility and coverage density, which can further reduce hardware requirements. Thus, while acquiring data from 200+ beams presents a technical challenge, it remains within the scope of modern embedded RF systems and scalable receiver design strategies.

VI. Conclusion

Massive MIMO antenna arrays are anticipated to equip LEO satellites, offering significant advantages for both telecommunication and positioning technologies. In this article, we presented our novel beam ID-based positioning method that uses the RF identifications of mMIMO beamforming loops that are incident from LEO satellite mega constellations. Through known geolocations of the beam footprint patterns and the suitable algorithmic treatment, the location of user terminals on Earth's surface can be determined to a precise-accurate extent, even by receiving beam(s) from one LEO satellite only in case of extreme conditions. We also developed an algorithm that utilizes the absent undetected beams for improved accuracy (ALG. B). The quality of positioning is substantially improved by increasing the number of LEO satellites in the skies, which in turn increases the amount of received beams. A detailed simulation environment was designed to comprise realistic LEO satellite constellation data and real-world navigation datasets. The conducted simulations showed a satisfactory level of performance for the fusion scheme that integrated LEO satellites data and IMU measurements. With the help of EKF-RTS algorithms and the moving average filter,

both the LEO/IMU fusion technique and the smoothed raw measurements achieved the best positioning estimations (in terms of accuracy and precision) that not only matched the typical performance of GNSS but also outperformed it. For both datasets I and II in the vanguard Scenario 4, the best error vector [MAE, RMSE, p95%] was evaluated at [9.15m, 11.94m, 19.07m], and [9.42m, 12.05m, 21.18m], respectively, against GNSS error vectors of [26.63m, 36.42m, 56.60m], and [18.55m, 22.24m, 36.38m], respectively. That is, an overall improvement in accuracy ranged from 70% to 205%. In the simulation, we explored larger antenna configurations in Scenario 4 such as 64×64, yielding more positioning accuracy, which is technically feasible in the next generation of LEO satellites. As future work, more refinements and model sophistication touches can be added to the simulation environment to improve the performance and integrity of the method. In addition, more research on positioning and post-processing algorithms is needed to reduce the number of LEO satellites required for conducting accurate UT positioning. The method presents several promising benefits in terms of sustainability and commercialization, which should be evaluated in future studies, e.g., through geospatial data analysis.

REFERENCES

[1] J. Khalife, M. Neinavaie, and Z. M. Kassas, "The first carrier phase tracking and positioning results with Starlink LEO satellite signals," *IEEE Trans. Aerosp. Electron. Syst.*, vol. 58, no. 2, pp. 1487–1491, Apr. 2022.

[2] C. Zhao, H. Qin, and Z. Li, "Doppler measurements from multiconstellations in opportunistic navigation," *IEEE Trans. Instrum. Meas.*, vol. 71, pp. 1–9, Feb. 2022.

[3] J. J. Morales and Z. M. Kassas, "Tightly coupled inertial navigation system with signals of opportunity aiding," *IEEE Trans. Aerosp. Electron. Syst.*, vol. 57, no. 3, pp. 1930–1948, Jun. 2021.

[4] Z. Tan, H. Qin, L. Cong, and C. Zhao, "Positioning using IRIDIUM satellite signals of opportunity in weak signal environment," *Electronics*, vol. 9, no. 1, p. 37, 2020.

[5] M. L. Psiaki, "Navigation using carrier doppler shift from a LEO constellation: TRANSIT on steroids," *Navigation*, vol. 68, no. 3, pp. 621–641, 2021.

[6] J. Xu, J. Y. Morton, D. Xu, Y. Jiao, and J. Hinks, "Tracking GNSS-like signals transmitted from LEO satellites and propagated through ionospheric plasma irregularities," in *Proc. 36th Int. Tech. Meeting Satell. Div. Inst. Navig. (ION GNSS+)*, 2023, pp. 1–19.

[7] A. L. Christovam, F. S. Prol, G. O. Jerez, M. Hernández-Pajares, and P. O. Camargo, "PPP at low latitudes with ionospheric model exclusively based on single frequency GNSS measurements," *Space Weather*, vol. 21, no. 8, 2023, Art. no. e2023SW003513.

[8] W. Kim and J. Seo, "Low-cost GNSS simulators with wireless clock Synchronization for indoor positioning," *IEEE Access*, vol. 11, pp. 55861–55874, 2023.

[9] J. Yun and B. Park, "A GNSS/barometric altimeter tightly coupled integration for three-dimensional semi-indoor mapping with android Smartphones," *IEEE Geosci. Remote Sens. Lett.*, vol. 21, Feb. 2024, Art. no. 8001005.

[10] A. Reda, T. Mekkawy, T. A. Tsiftsis, and A. Mahran, "Deep learning approach for GNSS jamming detection based PCA and Bayesian optimization feature selection algorithm," *IEEE Trans. Aerosp. Electron. Syst.*, vol. 60, no. 6, pp. 8349–8363, Dec. 2024.

[11] M. Ding, W. Chen, and W. Ding, "Performance analysis of a normal GNSS receiver model under different types of jamming signals," *Measurement*, vol. 214, Jun. 2023, Art. no. 112786.

[12] L. Bai, C. Sun, A. G. Dempster, H. Zhao, and W. Feng, "GNSS spoofing detection and mitigation with a single 5G base station aiding," *IEEE Trans. Aerosp. Electron. Syst.*, vol. 60, no. 4, pp. 4601–4620, Aug. 2024.

[13] F. S. Prol et al., "Position, navigation, and timing (PNT) through low earth orbit (LEO) satellites: A survey on current status, challenges, and opportunities," *IEEE Access*, vol. 10, pp. 83971–84002, 2022.

[14] W. Stock, R. T. Schwarz, C. A. Hofmann, and A. Knopp, "Survey on opportunistic PNT with signals from LEO communication satellites," *IEEE Commun. Surveys Tuts.*, vol. 27, no. 1, pp. 77–107, 1st Quart., 2024.

[15] H. More, E. Cianca, and M. De Sanctis, "Comparing positioning performance of LEO mega-constellations and GNSS in urban canyons," *IEEE Access*, vol. 12, pp. 24465–24482, 2024.

[16] S. Mostafa et al., "Vision: Leveraging low earth orbit satellites for future ubiquitous positioning," in *Proc. 32nd ACM Int. Conf. Adv. Geograph. Inf. Syst.*, 2024, pp. 473–476. [Online]. Available: https://doi.org/10.1145/3678717.3691251

[17] M. Elsanhoury, J. Koljonen, F. S. Prol, M. Elmusrati, and H. Kuusniemi, "Resilient navigation in GNSS-denied conditions using novel LEO-based fusion positioning," in *Proc. IEEE Int. Conf. Wireless Space Extreme Environ. (WiSEE)*, 2024, pp. 118–123.

[18] M. Elmusrati, M. Elsanhoury, J. Koljonen, and H. Kuusiniemi, "Method and system for positioning," U.S. Patent 20 235 545, May 2023. [Online]. Available: https://patenttitietopalvelu.prh.fi/en/patent/20235545/

[19] A. Florio, N. BniLam, C. Talarico, P. Crosta, G. Avitabile, and G. Coviello, "LEO-based coarse positioning through angle-of-arrival estimation of signals of opportunity," *IEEE Access*, vol. 12, pp. 17446–17459, 2024.

[20] J. Guo and Y. Wang, "Efficient AOA estimation and NLOS signal utilization for LEO satellite positioning," *Appl. Sci.*, vol. 15, no. 3, p. 1080, 2023.

[21] M. Elsanhoury, J. Koljonen, M. Elmusrati, and H. Kuusniemi, "A novel beam-based positioning paradigm via opportunistic signal of future massive MIMO LEO satellite constellations," Techrxiv, 2023, preprint. [Online]. Available: https://www.techrxiv.org/articles/preprint/A_Novel_Beam-Based_Positioning_Paradigm_Via_Opportunistic_Signal_of_Future_Massive_MIMO_LEO_Satellite_Constellations/23662578

[22] R. M. Ferre et al., "Is LEO-based positioning with mega-constellations the answer for future equal access localization?" *IEEE Commun. Mag.*, vol. 60, no. 6, pp. 40–46, Jun. 2022.

[23] J. Palacios, N. Gonzalez-Prelcic, C. Mosquera, T. Shimizu, and C.-H. Wang, "A hybrid beamforming design for massive MIMO LEO satellite communications," *Front. Space Technol*, vol. 27, Sep. 2021, Art. no. 696464.

[24] A. F. Molisch et al., "Hybrid beamforming for massive MIMO: A survey," *IEEE Commun. Mag.*, vol. 55, no. 9, pp. 134–141, Sep. 2017.

[25] O. E. Ayach, S. Rajagopal, S. Abu-Surra, Z. Pi, and R. W. Heath, "Spatially sparse precoding in Millimeter wave MIMO systems," *IEEE Trans. Wireless Commun.*, vol. 13, no. 3, pp. 1499–1513, Mar. 2014.

[26] M. Neinavaie and Z. M. Kassas, "Unveiling beamforming strategies of Starlink LEO satellites," in *Proc. Inst. Navig. GNSS+ Conf.*, 2022, pp. 2525–2531. [Online]. Available: https://people.engineering.osu.edu/media/document/2022-10-12/kassas_unveiling_beamforming_strategies_of_starlink_leo_satellites.pdf

[27] "Technical narrative: OneWeb ku-band NGSO system," OneWeb Satell. Commun., London, U.K., document SAT-MPL-20200526-00062, 2020. [Online]. Available: https://fcc.report/IBFS/SAT-MPL-20200526-00062

[28] J. Hartikainen, A. Solin, and S. Särkkä, *Optimal Filtering with Kalman Filters and Smoothers-A Manual for MATLAB Toolbox EKF/UKF*, Aalto Univ., Espoo, Finland, 2011.

[29] H. E. Rauch, F. Tung, and C. T. Striebel, "Maximum likelihood estimates of linear dynamic systems," *AIAA J.*, vol. 3, no. 8, pp. 1445–1450, 1965. [Online]. Available: https://doi.org/10.2514/3.3166

[30] M. Elsanhoury, J. Koljonen, P. Välisuo, M. Elmusrati, and H. Kuusniemi, "Survey on recent advances in integrated GNSSs towards seamless navigation using multi-sensor fusion technology," in *Proc. 34th Int. Tech. Meeting Satell. Div. Inst. Navig. (ION GNSS+)*, Sep. 2021, pp. 2754–2765.

[31] A. Howard et al. "Google smartphone decimeter challenge 2022." 2022. [Online]. Available: https://kaggle.com/competitions/smartphone-decimeter-2022

[32] A. Chow, D. Orendorff, M. Fu, M. Khider, S. Dane, and V. Gulati. "Google Smartphone Decimeter challenge 2023-2024." 2023. [Online]. Available: https://kaggle.com/competitions/smartphone-decimeter-2023

[33] J. R. Wertz, *Mission Geometry: Orbit and Constellation Design and Management: Spacecraft Orbit and Attitude Systems* (Space Technology Library). Portland, OR, USA: Microcosm Press, 2001.

[34] J. W. Harris and H. Stöcker, *Handbook of Mathematics and Computational Science*. New York, NY, USA: Springer, 1998. [Online]. Available: https://link.springer.com/book/9780387947464

[35] F. S. Prol et al., "Simulations of dedicated LEO-PNT systems for precise point positioning: Methodology, parameter analysis, and accuracy evaluation," *IEEE Trans. Aerosp. Electron. Syst.*, vol. 60, no. 5, pp. 6499–6516, Oct. 2024.
[36] C. Pinell, F. Prol, M. Bhuiyan, and J. Praks, "Receiver architectures for positioning with low earth orbit satellite signals: A survey," *EURASIP J. Adv. Signal Process.*, vol. 2023, p. 60, Jun. 2023, doi: 10.1186/s13634-023-01022-1.
[37] (COSPAS-SARSAT Council, Montreal, QC, Canada). *COSPAS-SARSAT 406 MHz Beacon Specifications*. 2020. Accessed: Jun. 8, 2025. [Online]. Available: https://www.cospas-sarsat.int/system-documents/beacon-specifications/406-mhz-beacon-specifications/
[38] (ORBCOMM Inc., Sterling, VA, USA). *ORBCOMM OG2 Satellite Network: Commercial IoT Connectivity*. 2025. Accessed: Jun. 8, 2025. [Online]. Available: https://www.orbcomm.com/en/partners/connectivity/satellite/og2
[39] (Defence Res. Develop. Canada, Ottawa, ON, Canada). *Resilience of Low Earth Orbit (LEO) Satellite Communications*. 2022. Accessed: Jun. 8, 2025. [Online]. Available: https://cradpdf.drdc-rddc.gc.ca/PDFS/unc500/p819264_A1b.pdf

Mahmoud Elsanhoury (Member, IEEE) received the B.Sc. degree in telecommunications engineering from Alexandria University, Egypt, in 2013, and the M.Sc. degree in telecommunications engineering and Ph.D. degree in computer science in 2018 and 2024, respectively. He is a Postdoctoral Researcher with the University of Vaasa, Finland. His doctoral research in LEO-PNT has attracted attention and recognition from regional and international institutions in Finland, Spain, and the USA. His current research interests include ubiquitous positioning systems, GNSS interference, indoor positioning systems, low Earth orbit satellite positioning or LEO-PNT, and multisensor fusion technologies. He is listed as one of the 10 Top Young Scientists in Finland 2023 by Technology Academy of Finland.

Janne Koljonen received the M.Sc. degree in automation technology from the University of Vaasa, Finland, in 2004, and the Ph.D. degree in automation technology in 2010. He has been involved in various research and teaching roles with the University since 2002. He is currently a Laboratory Engineer and a Programme Manager. He has authored more than 40 scientific articles.

Fabricio S. Prol received the Ph.D. degree in cartographic sciences from São Paulo State University, Brazil, with focus in geodetic remote sensing and geodetic positioning in 2019. He has been with the Finnish Geospatial Research Institute since 2021. His research interests include ionospheric modeling, GNSS positioning, LEO-PNT navigation, and data assimilation.

Mohammed S. Elmusrati (Senior Member, IEEE) received the B.Sc. (with Hons.) and M.Sc. (with High Hons.) degrees in electrical and electronic engineering from the University of Benghazi, Libya, in 1991 and 1995, respectively, and the Licentiate of Science in technology (with distinction) and the D.Sc. degrees in automation and control engineering from Aalto University, Finland, in 2002 and 2004, respectively. He is currently a Full Professor of Communication, Automation, and Digitalization with the School of Technology and Innovations—University of Vaasa, Finland. He has more than 145 publications, including articles, books, and book chapters. He is interested in various research topics, including wireless communications, AI, ML, biotechnology, big data analysis, stochastic systems, and game theory. He is an Active Member in different scientific societies, such as a Member at Society of Industrial and Applied Mathematics and Finnish Automation Society.

Heidi Kuusniemi (Member, IEEE) received the M.Sc. degree (Hons.) and the Ph.D. degree in information technology from Tampere University of Technology, Finland, in 2002 and 2005, respectively.

She is currently a Professor of Computer Science with the University of Vaasa, a Part-Time Research Professor with the Finnish Geospatial Research Institute, National Land Survey of Finland, and an Adjunct Professor of Satellite Navigation with Tampere University and Aalto University, Finland. She has more than 20 years of experience in research and development of positioning technologies and has held many significant positions of trust and expertise in the global scientific navigation community. She is the President of the Nordic Institute of Navigation. She is a member of the Finnish Academy of Science and Letters and the Finnish Academy of Technology, and she was a member of the Research Council for Natural Sciences and Engineering at the Research Council of Finland from 2019 to 2021. Her doctoral research was conducted at the Department of Geomatics Engineering, University of Calgary, Canada, from 2003 to 2004, and she was a Visiting Scholar with the GPS Laboratory, Stanford University, in 2017. Her research interests include GNSS, especially reliability, estimation and data fusion, mobile precision positioning with applications, indoor localization, and opportunities of PNT in new space.